

First Resolved Observations of the Demagnetized Electron-Diffusion Region of an Astrophysical Magnetic-Reconnection Site

J. D. Scudder,¹ R. D. Holdaway,¹ W. S. Daughton,² H. Karimabadi,³ V. Roytershteyn,³ C. T. Russell,⁴ and J. Y. Lopez¹

¹University of Iowa, Iowa City, Iowa 52442, USA

²Los Alamos National Laboratories, Los Alamos, New Mexico 87544, USA

³University of California, San Diego, La Jolla, California 92093, USA

⁴University of California, Los Angeles, Los Angeles, California 90095, USA

(Received 14 June 2011; published 1 June 2012)

Spatially resolved, diagnostic signatures across the X -line and electron-diffusion region (EDR) by the Polar spacecraft are reported at Earth's magnetopause. The X -line traversal has a local electron's skin depth scale. First, resolved EDR profiles are presented with peak electron thermal Mach numbers >1.5 , anisotropy >7 , calibrated electron agyrotropy >1 , and misordered expansion parameters indicative of demagnetization and strong (150 eV) increases in electron temperature. The amplitude and phase of these profiles correlate well with a guide geometry kinetic simulation of collisionless magnetic reconnection. Such high resolution diagnosis has been made possible by data processing techniques that afford an 11-fold reduction in the aliasing time for the electron moments.

DOI: 10.1103/PhysRevLett.108.225005

PACS numbers: 94.30.cp, 52.30.Cv, 52.35.Vd

Astrophysical energy releases, like solar flares, aurorae, and substorms, have been attributed since 1946 [1] to topological reorganizations of preexisting magnetic structures in plasmas permitted by localized dissipation in current channels. This reorganization, called “magnetic reconnection,” is facilitated in laboratory plasmas by binary collisions. For nearly collisionless astrophysical plasmas, the direct relevance of magnetic reconnection initially remained unclear. In 1975, a theoretical description for collisionless reconnection [2] was introduced that suggested the topology changes can occur at current layers approaching the scale of the thermal electron gyroradius, ρ_e , where nonideal corrections to the electron pressure tensor allow the frozen flux condition to be overcome. These considerations, involving the demagnetization of the electrons, suggested a current channel, called the electron-diffusion region (EDR), would form in this process with scales of order $d_i \times d_e$ where the k th species skin depth is $d_k \equiv (\frac{m_k c^2}{4\pi m_e e^2})^{1/2}$. In a plasma with equal electron, ion, and magnetic pressures, the EDR would have scales of order $\rho_i \times \rho_e$, where $\rho_k = \frac{w_k}{\Omega_{ck}}$ and w_k and Ω_{ck} are the thermal speed and cyclotron frequency of the k th species, respectively. The extent of electron demagnetization is reflected in the broken cylindrical symmetry of the electron pressure tensor, \mathbf{P}_e , about the magnetic field; a measure of this broken symmetry, called agyrotropy, is denoted by $A\emptyset_e$ [3]. In typical large-scale plasmas, demagnetization of electrons does not occur and $A\emptyset_e \approx 0$ is the accepted, integrated statement of the magnetization of electrons. In the last decade it has become possible to provide computational support for collisionless reconnection by using large-scale particle in cell (PIC) simulations [4], often with artificial particle masses, cyclotron to plasma frequency ratio, and idealized boundary conditions.

Observational signatures, such as Alfvénic acceleration layers, parallel electric fields or keV electron fluxes, have been interpreted as circumstantial evidence of the detection of reconnection (or even the EDR) in the solar wind, Earth's magnetosheath, and planetary magnetopauses [5–7].

We report the first *in situ* quantitative evidence for demagnetized thermal electrons within a resolved EDR in a collisionless astrophysical plasma. The detection uses five independent determinations, from three independent instrument suites [8], of the relevant short scales and integral measures of electron demagnetization that are the essential ingredients for how reconnection would be possible in low-density plasmas [2]. All five measured profiles are supported in size and spatial phasing by PIC simulations with similar dimensionless parameters. These signatures have such singularly large values, that in over 50 years of space plasma measurements they have never occurred separately, let alone in concert, as in this identification. These signatures reflect a plasma regime unique to collisionless reconnection, as benchmarked in the PIC simulations [9]. A recent 11-fold reduction in time aliasing of the Polar plasma instrument's computation of three-dimensional (3D) moments has allowed a greatly clarified diagnosis of the moving electron gyroscale structures involved. Since the needed plasma moments (see Supplemental Material [10]) involve low-order velocity-space spherical averages over only harmonics, Y_l^m with $l \leq 2$, relatively low-order Laguerre spherical harmonic fits can determine these moments from data acquired over 1.15 s from the instrument's unique, simultaneous sampling in all octants of velocity space [11].

The definitions and origin of the five dimensionless scalar diagnostics that were used to find the EDR are

distinct from those circumstantial signatures of reconnection or EDR that were previously used in the experimental literature. Together with the electromagnetic field, they involve either the electron bulk velocity, \mathbf{U}_e , and/or derived parameters, such as the pressure tensor, determined in the electron rest frame. They are: (i) energy gain per cyclotron period, $\epsilon_e \equiv \frac{2\pi e \mathbf{E} \cdot \mathbf{U}_e}{\Omega_{ce} k T_e}$, which is an expansion parameter of the guiding center theory (GCT) [9]; (ii) relative strength of electric and magnetic force in the electron fluid rest frame, $\delta_e \equiv \frac{|c\mathbf{E} + \mathbf{U}_e \times \mathbf{B}|}{w_{e\perp} B} \approx \frac{\rho_e}{L}$, another GCT expansion parameter [9]; (iii) agyrotropy of the measured electron pressure tensor, $A\mathcal{O}_e = 2 \frac{||-\alpha||}{(1+\alpha)} > 1$, where $\alpha \equiv P_{e\perp,1}/P_{e\perp,2}$ is the ratio of possibly distinct eigenvalues transverse to \mathbf{B} [3]; (iv) electron thermal anisotropy, $An_e \equiv \frac{T_{e\parallel}}{T_{e\perp}}$ lining the interface between the EDR and magnetospheric ion diffusion region (IDR) [12]; and (v) large electron thermal Mach number, $M_{e,\perp} \equiv \frac{|U_{e\perp}|}{\langle w_{e,\perp} \rangle} \approx O(1)$ [9], reflecting the needed ρ_e current channel of the EDR, where $\langle w_{e,\perp} \rangle$ is the electron thermal speed derived from the average perpendicular temperatures. We define κ_e to be the larger local value between δ_e and ϵ_e . It is also of interest that ϵ_e can depend on the perpendicular and parallel components of \mathbf{E} , especially when the electrons are demagnetized. A sixth correlative signature that is expected for the EDR, but not unique to demagnetization physics, is increased internal or suprathermal energy stored in the electrons.

From a 2D PIC simulation in the asymmetric guide geometry, we show in Fig. 1 an illustrative spatial profile

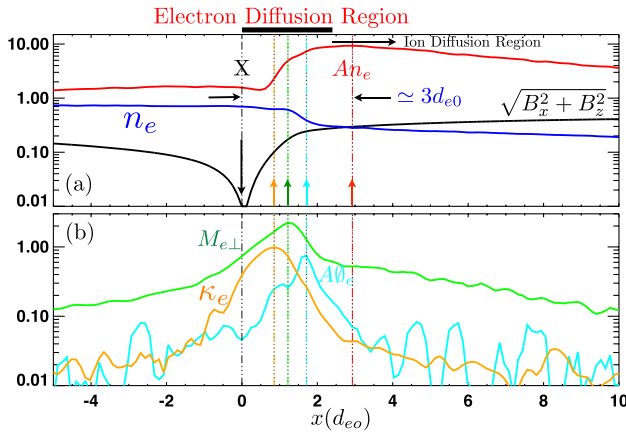


FIG. 1 (color online). PIC profiles through electron-diffusion region (indicated by thick horizontal black bar) passing through the separator ($x = 0$) showing (from top to bottom when $x < 0$) (a) profiles of An_e (red), n_e (blue), and the in-plane field components of \mathbf{B} (black), and (b) PIC diagnostics of electron inertial scale physics (with juxtaposed labels) $A\mathcal{O}_e$ (cyan), $M_{e,\perp}$ (green), and composite guiding center theory violation of expansion parameters, κ_e (orange). Arrows at peaks of same colored profiles. Phasing of peaks of X , $M_{e,\perp}$, $A\mathcal{O}_e$, An_e are shown in Polar data on the right-hand side of Fig. 3.

through the magnetic separator and across the EDR-IDR. The simulation had a guide field equal to the reconnecting field on the stronger field side of the layer used $T_i/T_e = 1$, $\frac{m_i}{m_e} = 100$, $\frac{\omega_{pe}}{\Omega_{ce}} = 2$, $\beta_{hi} = 1$, and $\beta_{lo} = 0.125$, where hi(lo) refer to the density of the asymmetric configuration. The equilibrium was achieved by the recently described method [13]. The separator (X -line) crossing ($x \equiv 0$) occurs where the reconnecting and normal components of \mathbf{B} simultaneously vanish [Fig. 1(a)]. Enhanced An_e requires adiabatic or magnetized electrons; thus, the peak of An_e [Fig. 1(a)] occurs just outside of the EDR-IDR interface, suggesting an EDR width of $\leq 3d_{eo}$. The signatures of demagnetized electrons [Fig. 1(b)] straddle the EDR, producing ordered enhancements of $\kappa_e \approx 1$, $M_{e,\perp} \approx 2$, $A\mathcal{O}_e \approx 0.75$, and $An_e \approx 7-8$, upon crossing the EDR-IDR boundary. The An_e profile extends asymmetrically into the magnetospheric IDR, but it is sharply attenuated on the separator side. $An_e(x)$ is sharply reduced when $A\mathcal{O}_e$ peaks. The peak of $M_{e,\perp}$ is closer to the magnetosheath than the peak of $A\mathcal{O}_e$. The GCT violations reflected in $\kappa_e \neq 0$ peak closer to and extend over the separator layer towards $x = -1$. Nonideal effects are seen at the separator, but the most intense signatures of demagnetization ($M_{e,\perp}$, $A\mathcal{O}_e$) occur toward the rear of the EDR, nearer to the low-density IDR boundary.

The reported event occurred near noon on May 4, 1998, as NASA's Polar spacecraft traversed the sunlit magnetopause at $9.0R_e$ at a magnetic latitude of 74.47° . As is typical at the magnetopause, the crossing had density and magnetic field strength asymmetries. Its guide magnetic field component was comparable to its shearing component and the layer encompassed a shear angle of 120° . The magnetic separator was observed straddling 12:03:05.5UT, as shown, versus time (space) in the left (right) column of Fig. 2. Figures 2(a)–2(c) support this identification, showing simultaneous (a) nulling of the shearing (z) and normal (x) components of \mathbf{B} , at the location (b) of strongly convergent normal component of E_x . Components are shown in a normal incidence minimum Faraday residue frame [14,15]. Within (± 40 s) of the identified separator crossing, framing signatures of enhanced energy transfer, $\epsilon_e \approx 0.25$, to the electrons is demonstrated and to be distinguished from the low values surrounding this region.

The relative velocity (1.6 km/s) of disturbances relative to the spacecraft was determined by the Faraday residue method [14], which permitted estimates of spatial distances used in Figs. 2(d) and 2(e). The magnetic shear angle, $\Sigma(x) \equiv \cos^{-1}[\mathbf{b}(\hat{\mathbf{x}}) \cdot \hat{\mathbf{b}}_0]$, advances in an orderly manner through 120° on the electron inertial scale, [Fig. 2(d)] within $\pm d_e^*$ of the separator, where d_e^* is one cumulative local electron skin depth from the separator, $d_e^* \equiv 0$. As theoretically expected, the B_z shearing components [Fig. 2(e)] decrease linearly with distance at different (β_e dependent) rates on either side towards zero.

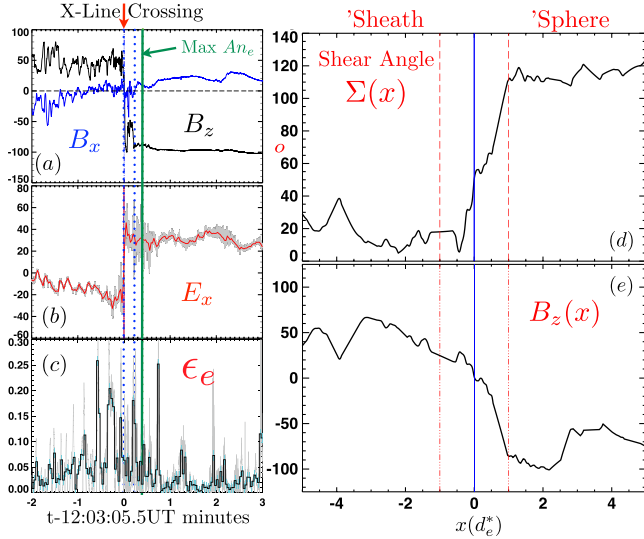


FIG. 2 (color online). *In situ* observations. Left column: time profile X-line vicinity in NIF, minimum Faraday residue coordinates showing measured (a) normal and shear magnetic components, $B_x(t)$, $B_z(t)$, and (b) the normal electric component $E_x(t)$ and (c) $\epsilon_e(t)$, the measured rate of work being done on the electrons per gyro period scaled by kT_e . Right: illustrates spatial profile of (d) the resolved X-line shear angle, $\Delta\Sigma(x) \approx 120^\circ$, and (e) interconnecting $B_z(x)$ variations within $\pm 5d_e^*$ about the separator X-line. Asterisk denotes cumulative number of such units from the X-line, $d_e^* = 0$. Grey shadows indicate variances about averages.

The one-hour plasma context surrounding the *in situ* separator crossing of Fig. 2 is shown in the left-hand column of Fig. 3. Initially in the magnetosheath, the spacecraft decisively enters the magnetosphere after 12:06UT. Several different lines of evidence suggest that the relative motion of the spacecraft before and after this magnetopause transit is not monotonic. Atypically large $An_e > 7$ is seen between 12:02:30 and 12:04:30, while spikes of An_e and other variables [left-hand side of Fig. 3] occur earlier and later than this time. A portion of the apparent time variability of the derived parameters may be caused by the nonuniform proximity and nonmonotonic advance of the spacecraft towards (away) from the sharp, d_e scaled separator shown in Fig. 2.

The very strong peak of $An_e(x)$ in the PIC profile in Fig. 1 and the large variations of $An_e(t)$ on the left-hand side of Fig. 3 suggest using the wide swings of the observed $An_e(t)$ to reorder the temporal measurements. The mapping uses $An_e(t)$ to produce Fig. 3(b) from Fig. 3(a). The rule divides the chronologically ordered vector \mathbf{V} , with elements $V_i = An_e(i\Delta t)$, into two smaller vectors \mathbf{V}_1 , \mathbf{V}_2 whose elements are those of \mathbf{V} for $i \leq k^*$ and $i > k^*$, respectively, where k^* is the index of the highest value of An_e within the strong ramp seen in the density in Fig. 3(i). The components of \mathbf{V}_1 are sorted to be monotonic, increasing in successive elements of the sorted vector \mathbf{SV}_1 , while

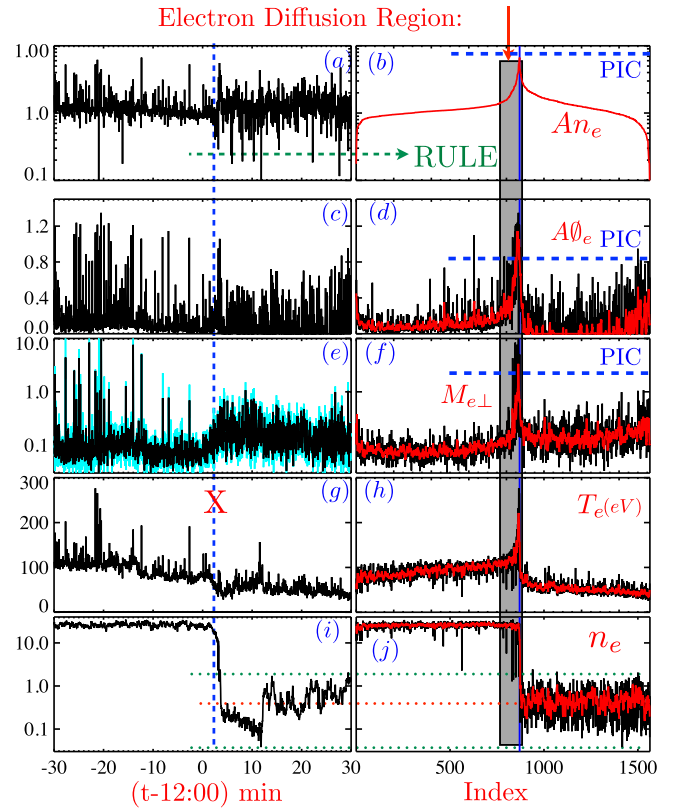


FIG. 3 (color online). Derived electron parameters across separator and EDR. The left column presents data in time order with X-line indicated by the vertical dotted blue line at 12:03:05.5UT. Panels in the right column are organized by a “rule” that reorders spectra indices by their increasing size of An_e to the left of the peak and, with decreasing order to the right, producing the smooth single peaked An_e profile in (b). Rule explained in text. This rule changes the temporal order in the left column, making smooth juxtapositions of similar An_e in the right column. The EDR is associated with the shaded rectangle in the right column, where coherent signatures of demagnetization, heating of electrons, and gyroscals are reinforced by this organization and achieve levels (horizontal dashed blue lines) predicted by and denoted “PIC.” Black traces are data at highest resolution. Red (thicker) traces are smoothed trends of black traces. Cyan (lighter) shadowing in (e) reflects $\pm 3\sigma$ uncertainties.

\mathbf{V}_2 is sorted into \mathbf{SV}_2 on the basis of monotonic decreasing size of $An_e(i > k^*)$. The result of the rule is the composite vector $\mathbf{SV} \equiv \mathbf{SV}_1 \oplus \mathbf{SV}_2$, which is plotted in its index order in Fig. 3(b). The rule between Fig. 3(a) and 3(b) is a map of indices i from the time domain variable to resorted indices $j(i)$ that can be used for any quantity measured with the same time cadence as $An_e(t)$. From this construction, it is clear that the means and extremes of \mathbf{V}_j and \mathbf{SV}_j are the same as illustrated between Fig. 3(i) and Fig. 3(j).

Under this rule, the horizontal axis on the left-hand side of Fig. 3 would become a monotonic, but nonuniform, spatial coordinate for the right-hand side of Fig. 3 if

$An_e(x)$ were known to be monotonic in space on either side of its peak value (blue vertical line). From Fig. 1, the PIC An_e profile is only slightly nonmonotonic near the separator, but it is monotonic throughout most of the EDR, including its extremely large values when $An_e \gg 1$. This rule juxtaposes similar regimes of An_e and allows an experimental assay of the spatial phasing of other observables with respect to the peak of An_e . At lower values of anisotropy, especially where $An_e < 1$, the rule for the x axes of the right-hand side of Fig. 3 separates spatial layers having large ∇An_e that might spatially be very “close” to those of high An_e .

The rule maps within rows the black curves on the left-hand side of Fig. 3 into the black curves on the right-hand side of Fig. 3. Localized but sharp transitions are revealed on the right-hand side of Fig. 3 in the electron observables. Strong narrow peaks in with (i) mean energy $T_e \approx 300$ eV, (ii) $An_e \approx 8$, (iii) $M_{e\perp} \approx 1.5$, (iv) $A\varnothing_e > 1$, and a newly clarified step in the density [Figs. 3(i) and 3(j)] astride the maximum An_e peak, consistent with the PIC profiles of Fig. 1. The general coherence and reduced structure of the panels on the right-hand side of Fig. 3 suggests that much of the spikiness of the left-hand column of Fig. 3 is not caused by the new method that has improved the plasma data’s time resolution 11-fold [10].

The coherence produced on the right-hand side of Fig. 3 warrants the smoothing (red curves) to compare trends. The peaks of the trends of $M_{e\perp}$ and $A\varnothing_e$ lead An_e when using the index number to order the data as in the right-hand panels of Fig. 3. The levels of the coherent demagnetization signatures compare favorably with those from PIC (dashed horizontal blue lines). Two degenerate candidates emerge for the wide swings in the higher time resolution measurements of the left-hand side of Fig. 3: (i) multiple encounters with one cohesive narrow structure induced by changing relative velocities of spacecraft and magnetopause during the crossing, and (ii) encounters with many smaller structures with similar plasma properties. The separatrices emanating from the EDR in PIC are often different from the usual large radius of curvature X patterns of theoretical cartoons. Both sides of Fig. 3 admit the interpretation of multiple encounters with EDR-like properties for a lengthy period both prior to and after the irreversible entry into the magnetosphere. Alternatively, recent 3D simulations of reconnection [16] have suggested that the EDR spawns multiple current channels, making crossings likely of many very narrow, possibly self-similar fiber-like layers from the main EDR layer.

The coherence within the shaded region in the right-hand side of Fig. 3 constitutes direct experimental support for nonideal electron effects as enabling demagnetized thermal electrons in the current channel. The phase coherent signature of large $An_e > 7$ layers with peak amplitudes comparable to that in PIC [dashed blue line Fig. 3(b)], together with the simulation overview that such layers

mark the EDR-IDR boundary on the magnetospheric side of asymmetric layers, provides further strong support for our EDR identification from the adjacent demagnetized layers seen in the shaded rectangle on the right-hand side of Fig. 3. The sharply enhanced electron temperature (at the boundary) in the shaded layer is nearly 150 eV higher than the larger of the two asymptotic temperatures, representing the first detection of electron heating associated with traversal of a documented reconnection site and should be contrasted with its reported absence in interplanetary events interpreted to be those of reconnection [6]. The present analysis also provides possible support for the emerging view in 3D simulations that the EDR layer may bifurcate into many smaller demagnetized current channels that the Polar may have intercepted on the left-hand side of Fig. 3. The An_e ordering afforded on the right-hand side of Fig. 3 suggests new ways to organize the emerging 3D picture of reconnection. The detection of the elusive signatures of electron heating and extreme electron $P_{e\parallel} \gg P_{e\perp}$ anisotropy confirm the role of parallel potentials and electron trapping physics in the EDR and its proximity [12].

Five observed diagnostics, using three autonomous experiments on the Polar spacecraft have been shown to coordinate well with the amplitude, phase, and extent of simulation spatial profiles known to describe the process of collisionless reconnection. The extraordinarily high thermal Mach numbers, anisotropy, and agyrotropy are so singular in the history of space physics that they require a singular phenomena to explain them. These signatures constitute strong direct experimental evidence of the first detection of the nonideal demagnetized EDR in a collisionless astrophysical plasma.

We acknowledge support from Grants No. NNX07AF64G, No. NNX07AF54G, No. NNX12AI20G, and No. ATM0802380. W.D. was supported by the NASA Heliospheric Theory Program. Calibrated 3-axis Polar EFI data and discussions with F.S. Mozer are gratefully acknowledged. NSF Kraken and NASA Pleiades supercomputers were used.

-
- [1] R. G. Giovanelli, *Nature (London)* **158**, 81 (1946).
 - [2] V. M. Vasyliunas, *Rev. Geophys. Space Phys.* **13**, 303 (1975).
 - [3] J. D. Scudder and W. Daughton, *J. Geophys. Res.* **113**, A06222 (2008).
 - [4] M. Hesse, K. Schindler, J. Birn, and M. Kuznetsova, *Phys. Plasmas* **6**, 1781 (1999); P. L. Pritchett, *J. Geophys. Res.* **106**, 3783 (2001); W. Daughton, J. D. Scudder, and H. Karimabadi, *Phys. Plasmas* **13**, 072101 (2006); H. Karimabadi, W. Daughton, and J. D. Scudder, *Geophys. Res. Lett.* **34**, L13104 (2007).
 - [5] G. Paschmann, *Geophys. Res. Lett.* **35**, L19109 (2008).
 - [6] J. T. Gosling, *Space Sci. Rev.*, doi:10.1007/s11214-011-9747-2 (2011).

- [7] F. S. Mozer *et al.*, *J. Geophys. Res.* **116**, A12224 (2011).
- [8] C. T. Russell, R. C. Snare, J. D. Means, D. Pierce, D. Dearnorn, M. Larson, G. Barr, and G. Le, *Space Sci. Rev.* **71**, 563 (1995); P. Harvey *et al.*, *Space Sci. Rev.* **71**, 583 (1995); J. D. Scudder *et al.*, *Space Sci. Rev.* **71**, 459 (1995).
- [9] J. D. Scudder *et al.*, *Phys. Plasmas* (to be published).
- [10] See Supplemental Material at <http://link.aps.org/supplemental/10.1103/PhysRevLett.108.225005> for description of the method.
- [11] J. D. Scudder *et al.*, *Space Sci. Rev.* **71**, 459 (1995).
- [12] A. Le, J. Egedal, W. Daughton, J. F. Drake, W. Fox, and N. Katz, *Geophys. Res. Lett.* **37**, L03106 (2010).
- [13] V. Roytershteyn, W. Daughton, H. Karimabadi, and F. S. Mozer, *Phys. Rev. Lett.* **108**, 185001 (2012).
- [14] A. Khrabrov and B. U. Ö. Sonnerup, *Geophys. Res. Lett.* **25**, 2373 (1998).
- [15] C. C. Goodrich and J. D. Scudder, *J. Geophys. Res.* **89**, 6654 (1984).
- [16] W. Daughton, V. Roytershteyn, H. Karimabadi, L. Yin, J. Albright, B. Bergen, K. J. Bowers, *Nature Phys.* **7**, 539 (2011).